Journal of Materials Chemistry A

Accepted Manuscript

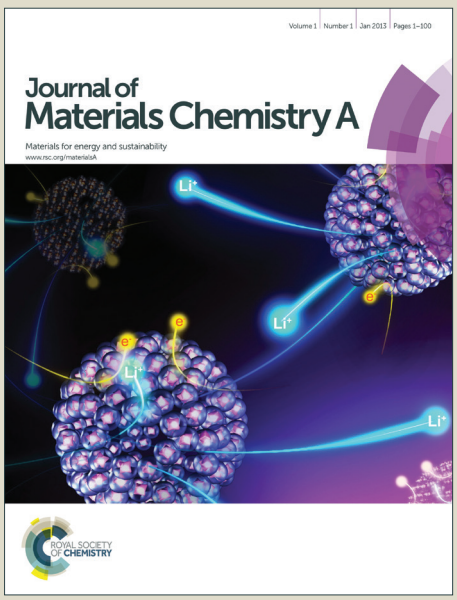

ROYAL SOCIETY OF CHEMISTRY

www.rsc.org/materialsA

Journal of Materials Chemistry A

PAPER

An All-Conjugated Gradient Copolymer Approach for Morphological Control of Polymer Solar Cells

Received 00th January 20xx,
Accepted 00th January 20xx

DOI: 10.1039/x0xx00000x

www.rsc.org/

Jojo A. Amonoo,[a] Anton Li,[b] Geoffrey E. Purdum,[c] Mathew E. Sykes,[b] Bingyuan Huang,[b] Edmund F. Palermo,[d] Anne J. McNeil,[d] Max Shtein,[b] Yueh-Lin Loo[c] and Peter F. Green*[ab]

This work introduces fully π-conjugated gradient copolymers as promising materials to control and stabilize the nanoscale morphology of polymer:fullerene solar cells. Gradient and block sequence copolymers of 3-hexylselenophene (3HS) and 3-hexylthiophene (3HT) are utilized as the donors (D) in bulk-heterojunction (BHJ) solar cells with phenyl-C61-butyric acid methyl ester (PCBM) as the acceptor (A). We show that for the same overall copolymer composition, the ordering of molecular constituents along the copolymer chain (copolymer sequence) significantly influences the nanoscale morphology and phase separation behavior of π-conjugated copolymer:fullerene devices. In addition, energy-filtered transmission electron microscopy (EFTEM) of the blends revealed that relative to the block copolymer:PCBM, the gradient copolymer:PCBM sample formed a more uniform, continuous and interconnected network of polymer fibrils within the acceptor-rich phase, associated with a large D/A interface. Charge extraction of photogenerated carriers by linearly increasing voltage (photo-CELIV) shows that the gradient copolymer:PCBM device possesses the highest initial carrier density, $n(0)$ = (3.92 ± 0.3) x 10^{18} cm^{-3}, consistent with a larger D/A interfacial area suggested by the observed morphology, albeit at the expense of increased carrier recombination rate. Accelerated degradation studies show that the gradient copolymer:PCBM system maintains the highest efficiency over prolonged heat treatment.

Keywords: conjugated gradient copolymer, organic solar cells, morphology, thermal stability

1. Introduction

Conjugated polymer:fullerene bulk-heterojunction (BHJ) systems offer a low-cost avenue to flexible thin-film solar cell technology. The overall device performance is inextricably linked to the three-dimensional molecular arrangement of the active materials; nanoscale morphology plays a critical role in the exciton dissociation and charge transport processes. For a particular blend system, improvement in power conversion efficiency (PCE) is typically achieved by controlling phase-separation length scales using post-production protocols (annealing) or high boiling-point solvent additives.[1, 2] The optimum nanoscale morphology consists of donor/acceptor (D/A) domains on the order of the exciton diffusion length (~10 nm), and large interfacial area in the bulk associated with D/A phases forming percolated networks facilitating charge separation and transport.[3] This putatively ideal morphology is not the true thermodynamic equilibrium morphology, but rather a kinetically trapped metastable structure. Hence, polymer solar cell device performance generally degrades upon extended processing or aging as the system approaches a more stable, and less favorable, morphology unless a compatiblizer is introduced to arrest the kinetically trapped morphology.[4, 5] For the extensively studied P3HT:PCBM system, prolonged processing increases the domain size of the fullerene aggregates, leading to a reduction in D/A interfacial area and ultimately reduces PCE.[6]

[a] Applied Physics Program, University of Michigan, Ann Arbor, MI 48109, USA.
[b] Department of Materials Science and Engineering, University of Michigan, Ann Arbor, MI 48109, USA
[c] Department of Chemical and Biological Engineering, Princeton University, Princeton, NJ 08544, USA.
[d] Department of Chemistry, University of Michigan, Ann Arbor, MI 48109, USA.
* E-mail: pfgreen@umich.edu
Electronic Supplementary Information (ESI) available: [details of any supplementary information available should be included here]. See DOI: 10.1039/x0xx00000x

For this reason, significant research has been geared towards improving the long-term thermal stability of polymeric solar cells. The active layer microstructure is often described as a combination of ordered polymer-rich domains, fullerene-rich aggregates and mixtures of molecularly dispersed fullerene in disordered polymer regions.[7] Most of the efforts to improve thermal stability have focused on suppressing phase separation and stabilizing polymer/fullerene interfaces in the active layer using photo-crosslinkable conjugated polymers,[8] thermally stable copolymers,[9-11] copolymer and molecular additives as suitable compatibilizers[4, 5, 12] and donor polymers low in regioregularity.[13]

Recently, the use of rod-rod π-conjugated copolymers in BHJ polymeric solar cells as either the primary donor material or additives serving as nanostructuring agents has garnered significant interest as an effective method to control nanoscale morphology, promote phase separation, and improve thermal stability.[11, 14, 15] However, none of these has included the use of fully π-conjugated gradient sequence copolymers as the main donor species. Besides their inherent ability to self-assemble into well-defined nanostructures, copolymers offer the additional advantage of fine-tuning physicochemical properties through advanced synthetic chemistry of the constituent molecules, thus providing opportunities for further improvement. While methods for synthesizing coil-coil gradient copolymers with precise composition profiles have existed,[16, 17] it is only recently that nickel-catalyzed "living" chain growth polycondensation techniques have enabled exquisite control of the copolymer chain architecture and comonomer sequence distribution of π-conjugated systems.[18-20] For example, π-conjugated gradient copolymers, whose instantaneous composition varies gradually along the polymer chain (Fig. 1), are now accessible by these emerging methods.[20-23]

Gradient copolymers exhibit a unique set of physical and morphological properties generally intermediary between that of the block copolymer (Fig. 1), which possesses a step change in composition, and the random copolymer, which possesses a uniform composition profile along the polymer chain.[5, 24-26] Furthermore, gradient copolymers have been shown to be effective interfacial modifiers, offering a larger degree of control over the interfacial profile in polymer blends.[27] Gradient copolymers have numerous uses spanning applications as blend compatibilizers,[27, 28] damping materials,[29] and thermoplastic elastomers.[30] Recently, π-conjugated gradient copolymers containing 3-hexyl selenophene (3HS) and 3-hexyl thiophene (3HT) units were introduced and it was found that poly(3-hexylselenophene-*gradient*-3-hexylthiophene) P(3HS-*g*-3HT) displayed distinctive physical, optical and thermal properties compared to the block, poly(3-hexylselenophene-*block*-3-hexylthiophene) P(3HS-*b*-3HT), and random poly(3-hexylselenophene-*random*-3-hexylthiophene) P(3HS-*r*-3HT) analogs.[21]

In this study, to gain a deeper understanding into the role of molecular sequence along the copolymer chain and structure-property-performance relationships of π-conjugated copolymers, we evaluate the nanoscale morphology, thermal stability and device performance of P(3HS-*g*-3HT) and P(3HS-*b*-3HT) as donor materials in polymer:fullerene photovoltaic systems. From energy-filtered transmission electron microscopy (EFTEM) measurements, the gradient copolymer device shows a continuous interconnected fibril network relative to the block architecture, suggesting a larger interfacial area in the bulk between the polymer and fullerene components. This result is further corroborated by carrier dynamics measurements using photo-CELIV where we found that the gradient copolymer device generated the highest initial carrier density. Furthermore, an accelerated degradation test revealed the gradient copolymer device to be the most robust, maintaining the highest optimum performance with prolonged annealing.

2. Results and Discussion

The P(3HS-*g*-3HT) and P(3HS-*b*-3HT) copolymers used in this study were synthesized and characterized using previously published procedures (see supporting information for details).[21] Fig. 1 shows the chemical structure of the homopolymers and copolymers with a schematic of the copolymer chain architecture. In the gradient design, the block-like chain ends are covalently linked by a gradual change in comonomer composition along the copolymer chain. A physical blend of the two homopolymers (P3HS:P3HT) in a 1:1 mass ratio was used for comparison to elucidate the importance of molecular ordering along the polymer chain. The molecular weight distributions, number-average molecular weights and regioregularity of all polymers used were nearly identical to isolate the effect of copolymer chain sequence, see Table S1. For the copolymers, molar compositions of the comonomers were approximately 1:1. Devices were fabricated in the inverted device architecture for stability under ambient conditions.[31]

2.1. Absorption Spectra of Thin Films and Device Spectral Response

We first studied the photophysical properties of the optimized polymer:fullerene blends using UV-visible spectroscopy. Fig. 2 shows the normalized absorption spectra where the wavelength range is selected to highlight the absorption profile of the polymers. We found that P3HS absorption is significantly red-shifted from that of P3HT, consistent with other studies and the fact that P3HS has a lower band gap.[32, 33] Both P3HT and P3HS polymers show characteristic vibronic structures manifested as strong absorption shoulders near 610 nm and 700 nm respectively, associated with π-aggregation and strong interchain interaction.[33, 34] The P(3HS-*b*-3HT) copolymer showed an almost identical absorption profile to the homopolymer blends of P3HS:P3HT (1:1) suggesting the existence of phase separation between the P3HS-block and P3HT-block in the block copolymer[35] and that P3HS and P3HT are thermodynamically incompatible. For the P(3HS-*g*-3HT), we observed weak absorption features associated with 3HT and 3HS chain interaction at 610 nm and 700 nm. This apparent reduction of π-aggregation in the P(3HS-*g*-3HT):PCBM films suggests that, relative to the block copolymer, the composition gradient along the polymer chains disrupts the thiophene-thiophene and selenophene-selenophene π-interactions and that alignment and packing may be constrained to the chain termini. This result was the same in the annealed neat P(3HS-*g*-3HT) film (not shown here). External quantum efficiency (EQE) measurements were performed and compared to the absorption profiles. EQE plots are shown in Fig. 3. We note that even though the absorption spectra of P(3HS-*b*-3HT) and the 1:1 blend are almost identical, their spectral response is very dissimilar both in the P3HT (400 nm – 650 nm) and non-P3HT absorbing regions (650 nm – 750 nm). The data shows that photon harvesting is decreased in both P3HT-block and P3HS-blocks in P(3HS-*b*-3HT):PCBM device. Even though the copolymers have comparable comonomer molar compositions, interestingly, the intensity of the EQE spectra of P(3HS-*g*-3HT):PCBM and P(3HS-*b*-3HT):PCBM vary markedly in the P3HT absorbing region but are similar in the 650 nm - 750 nm wavelength range. These results suggest the composition gradient in the donor copolymer improves photon harvesting in the P3HT absorbing region.

2.2. Bulk Heterojunction Device Performance and Thermal Stability

Having shown that the optical properties of the homopolymers can be tailored by finely adjusting the copolymer sequence, we proceeded to evaluate their performance in photovoltaic devices. Each polymer:fullerene device was optimized independently, especially with regards to weight fraction of the active materials and fabrication procedure. For the gradient and block copolymers, the optimum copolymer:fullerene mass ratio was the same at 55:45. Details can be found in the experimental section. Representative J-V curves under 1-sun simulated solar illumination displayed typical diode-like behaviour as shown in Fig. 4. For all optimized devices, P3HT:PCBM was still the

"champion" (3.7 ± 0.1%). Interestingly, the P(3HS-*g*-3HT):PCBM device performed reasonably well (3.3 ± 0.1%), whereas the P(3HS-*b*-3HT):PCBM and P3HS:PCBM devices were less efficient. We then designed a series of thermal stability experiments to further understand the relationship between the active layer microstructure and performance. The evolutions of the PCE, short circuit current density (J_{SC}), open circuit voltage (V_{OC}) and fill factor (*FF*) as a function of annealing time at 150˚C are highlighted in Fig. 5. We will discuss the V_{OC} trend in relation to charge carrier decay dynamics later. For each materials pair, at least 9 devices were measured, yielding the error bars. We clearly see that all P3HS-based devices demonstrate superior thermal stability over long annealing times in contrast to the P3HT-only device, which steadily declines in performance after reaching a maximum after 15 min. Previous studies of P3HS:fullerene mixtures have shown that during thermal treatment, there exists a higher fraction of disordered polymer phase in P3HS:PCBM films even though P3HS packs much better and forms high quality crystallites relative to P3HT in P3HT:PCBM blends.[36] The presence of a higher amount of P3HS amorphous phase tends to facilitate the mixing of PCBM molecules and thereby suppresses PCBM aggregation.[36] This is in contrast to the P3HT:PCBM system where phase separation continues with annealing leading to lower PCE, as shown in Fig. 5a. The most straightforward explanation is that the 3HS components become more miscible with PCBM upon thermal annealing, stabilizing the morphology and preventing further phase separation. It is also noteworthy that the melting temperature (T_m) of P3HT ($T_{m,\ P3HT}$ = 243˚C) is lower than that of P3HS ($T_{m,\ P3HS}$ = 256˚C),[21] which possibly reflects differences in chain mobility at the annealing temperature of 150˚C. These results demonstrate that the composition gradient along the copolymer chain in the P(3HS-*g*-3HT):PCBM offers a morphology that stabilizes the D/A interface while simultaneously providing the optimum nanostructure required for charge separation and collection.

2.3. Polymer Crystallization: GIXD

We employed grazing-incidence X-ray diffraction (GIXD) to probe the long-range intermolecular order and crystallinity of the optimized polymer:fullerene samples. The two-dimensional GIXD patterns and the normalized intensity traces taken at q_{xy} = 0 associated with the polymer donors in the samples are shown in Fig. 6. The GIXD patterns clearly show that the homopolymers, blends, and copolymers all self-organize into periodic lamellar structures; that the intensities of the (h00) reflections of P3HT and P3HS are concentrated along the meridian indicates that the polymer crystallites are preferentially oriented in an edge-on fashion.[37] Taking a line cut of the two-dimensional GIXD patterns at q_{xy} = 0 yields one-dimensional X-ray trace representative of the out-of-plane reflections (Figs. 6f and 6g). The traces associated with the P3HT and P3HS homopolymers reveal the (100) reflections at 0.38 Å-1 and 0.41 Å-1, respectively, consistent with a prior report.[38] The line trace of the film comprising a blend of both P3HT and P3HS reveal reflections associated with both polymer donor constituents, as seen most clearly by distinct (200) reflections (Fig. 6g). Interestingly, the GIXD images of both the block and gradient copolymers also reveal evidence of coexistence of crystallites of both polymer donor constituents; this can be best seen in the vertical line traces of the (200) reflections in Fig. 6g in which the x-ray intensities in this q-range can be fitted to two Gaussians with centers corresponding to the (200) reflections associated with P3HT and P3HS homopolymers. The fractional intensities corresponding to each Gaussian can thus be used as a proxy for the relative crystallinity of 3HS and 3HT, and obtain a relative measure of the lamellar packing order. Carrying out this analysis reveals that, of the crystalline portions of the 1:1 blend and copolymer films, only 10-20% can be attributed to 3HT. This analysis suggests that for all annealed samples, the 3HS components exhibit enhanced fractional crystallinity related to the packing order of the lamellar compared to the 3HT segments within the homopolymer blend and copolymer films with PCBM. In other words, the 3HS crystalline phase comprises of

higher quality crystals of enhanced lamellar packing order than the 3HT crystalline phase.

Recent studies have shown that in an all-conjugated block copolymer system, phase separation is induced by the identity of the heterocycle.[35] Even though the exact interaction between the two blocks during crystallization is not yet well understood, it has been suggested that in these highly rigid-rod-like block copolymers, the first block to crystallize would be the one with the highest T_m.[39] In this instance, the microphase-separated structure would be dictated by this block, which could confine the crystallite size and domains of the other block. Since $T_{m,\ P3HT} < T_{m,\ P3HS}$ we can thus reasonably infer that the 3HS block/segment is likely to initiate crystallization of the copolymer, and as a result, further constrain the crystallization of the covalently-bound 3HT block/segments. Consequently, differences in the spatial arrangements and locations of 3HS components along the copolymer chain influence the crystallization behaviour leading to differences in nanoscale morphology as will be discussed in the following section.

2.4. Active-Layer Morphology Characterization: EFTEM

The nanoscale morphology of the optimized polymer:fullerene samples was studied using energy-filtered transmission electron microscopy (EFTEM) to distinguish between polymer and fullerene-rich phases.[40] After taking the spectral images, an energy-loss window was selected to maximize contrast in scattering intensity between the phases; the images in Fig. 7 were integrated over the energy-loss range of 31.5 ± 3 eV such that the PCBM-rich regions appear bright and the polymer fibrils/domains appear dark. A qualitative comparison between the P(3HS-*b*-3HT):PCBM and P(3HS-*g*-3HT):PCBM samples reveals that the gradient copolymer forms a more uniform and continuous network of polymer fibrils within the fullerene-rich phase, which would be associated with facile carrier transport and a large D/A interface for exciton dissociation. On the other hand, the fibrils formed by the block copolymer assemble into dense clusters separated by large fullerene-rich regions with sparse fibrils. This type of meso-scale organization suggests a smaller D/A interfacial area and fewer continuous pathways for hole transport. Furthermore, this result shows that the gradient architecture tends to mitigate the intrinsic self-assembly characteristic of its block copolymer analog. One way to explain this observation is to first recall that the gradient sequence disrupts the strong interaction between 3HS and 3HT components in the block architecture, with 3HS being the precursor for the copolymer crystallization process. For the gradient copolymer, inter-chain π-interactions between selenophene-selenophene segments are restricted to the chain ends, which are block-like (see Fig. 1). Additionally, the gradual change in composition along the chain results in a weaker interaction between the segments near the chain center, resulting in an inhibition in self-assembly for the gradient copolymer in comparison with the block copolymer, as shown. A similar effect was reported in recent work by Seferos and co-workers of the statistical variant, P(3HS-*s*-3HT), in which the statistical distribution of the comonomers along the chain were shown to interrupt the strong interaction between 3HS components leading to improved solubility and an extreme reduction in structural order relative to the block copolymer.[41] With regards to our results, it is evident that the gradient copolymer provides morphological characteristics that are intermediate between the statistical copolymer, where vapor annealing is required to improve the nanosclae order, and the block copolymer, which undergoes intrinsic phase separation.

In addition, simulations of the microphase separation characteristics of gradient and symmetric block copolymer thin films that form lamellae have shown that the physics of self-assembly between the two systems are fundamentally different even for the same lamellar period.[42, 43] For linear gradient copolymers, variations in composition along the chain results in an A-B monomer interaction that drives A-rich and B-rich chain termini from the comonomers at the relatively broad region of the chain center.[42] In contrast, for the block copolymer, the A-B monomer

interfacial regions are localized to the narrow interface of the chain junction.[42] A natural occurrence of the structure is that, at very high χN, gradient copolymers exhibit much weaker phase segregation relative to their block copolymer counterparts which possess a much narrower interfacial region.[43] These simulations are consistent with our EFTEM studies; the strong and weaker interaction between the chain ends and center respectively tends to influence the crystallization behavior which increases the interfacial area between the gradient copolymer and fullerene resulting in a higher D/A interfacial area and in the process generated the highest initial carrier density which will be discussed in the next section. Because, the block copolymer device exhibited a stronger tendency to phase segregate, leading to less D/A interfacial area, the lowest initial carrier densities were measured. Although it is not obvious at the scale/resolution of images in Fig. 7, the P3HT:PCBM sample possesses finer fibrillar features than the copolymers (see Supporting Information for higher magnification image). The P3HS:P3HT:PCBM blend shows large and poorly-defined "patches" of polymer-rich/fullerene-rich regions, consistent with the existence of phase-separated "domains" of P3HS:PCBM and P3HT:PCBM.

2.5. Carrier Dynamics

To gain information about carrier generation and recombination, devices were characterized using photo-CELIV. In this technique, the transient current generated by a 532 nm laser pulse excitation is measured at various delay times and a linearly increasing voltage applied to extract the carriers yielding a photo-generated carrier density. Fig. 8 shows plots of charge carrier density versus delay time for optimum devices studied. All devices showed a decrease in carrier density as delay time increased reminiscent of recombination in the active layer. Since the curves exhibit a power law dependence with time, $n(t) \propto t^{\alpha}$, we fit the data sets to the power law formula and extrapolated to t=0 to obtain the initial carrier density, n(0), for each device. The data obtained is as follows: P3HT:PCBM, n(0) = (1.34 ± 0.3) x 10^{17} cm^{-3}, P3HS:PCBM, n(0) = (1.48 ± 0.3) x 10^{17} cm^{-3}, P(3HS-*b*-3HT):PCBM, n(0) = (5.54 ± 0.3) x 10^{16} cm^{-3}, and P(3HS-*g*-3HT):PCBM, n(0) = (3.92 ± 0.3) x 10^{18} cm^{-3}. Not surprisingly, the initial carrier density of the gradient copolymer device is two orders of magnitude higher than the block copolymer. In fact, the gradient copolymer device showed the highest initial carrier density among all the devices consistent with the active layer of the gradient copolymer:PCBM having a much more continuous and interconnected fibril network, such as that shown in Fig. 6. With the highest initial carrier density, one might ask why then does the gradient copolymer device not out-perform the P3HT:PCBM "champion"? The answer lies in the free carrier recombination rates, which were extracted from the α exponent. The values are as follows: P3HT:PCBM, α = -0.80 ± 0.04 , P3HS:PCBM, α = -2.10 ± 0.01, P(3HS-*b*-3HT):PCBM, α = -1.45 ± 0.03 , and P(3HS-*g*-3HT):PCBM, α = -2.25 ± 0.03. This result suggests that carrier recombination is most prevalent in the gradient copolymer device but for this device to maintain a decent performance, suggests that the large initial carrier generation compensates immensely for the numerous free carrier losses. In polymer:fullerene devices, recombination studies performed near open-circuit conditions have shown that V_{OC} and *FF* are limited primarily by nongeminate recombination.[44-47] The fact that even with higher recombination rates in the optimum gradient copolymer device its V_{OC} (0.6 V) and that of the P3HT device (0.6 V) are identical is suggestive of the existence of trap-assisted recombination in the gradient copolymer device.[44] Considering that the energetic landscape is influenced by variations in local ordering of the polymer structure driven by variations in conjugation length and also the magnitude of intermolecular interactions between polymer and fullerene,[48, 49] it is likely that the differences in molecular arrangements and interactions between the 3HT, 3HS and fullerene components for each of the systems studied vary and would influence the interplay between nanoscale morphology and electronic structure which ultimately affects the density of trap sites or recombination centers. One way to explain this result is that the gradient copolymer device provides a

decent trade-off between the high initial carrier density and recombination, by providing enough charge carriers to fill these trap states while leaving an adequate amount available for transport and extraction at the respective electrodes.

2.5. Local Photocurrent Mapping

Having studied the optical properties, nanoscale morphology, crystallinity and carrier dynamics of our films and devices, it is now instructive to examine the local photocurrent generation using photoconductive atomic force microscopy (pcAFM). The samples were excited using a 532 nm diffraction limited laser and measurements performed at 0 V bias. Details of the pcAFM experiments can be found in the experimental section. These measurements were done on the same samples that were used for the bulk J-V measurements and scans were taken in areas between the top electrodes. Fig. 9 shows the photocurrent maps of all the samples. This result gives us an insight into why the P(3HS-*b*-3HT):PCBM performed poorly. We clearly see larger regions exhibiting low to no photoconductivity at all compared to all the other samples. We hypothesize that these regions are block copolymer-rich domains that have self-assembled and in the process excluded PCBM molecules, resulting in a decrease in the D/A interfacial area which leads to a decrease in photocurrent collection, low J_{SC} and *PCE*. This result further corroborates the dense clusters of fibrils observed in the EFTEM images, which we concluded were the phase separated block copolymer-rich phase. Also, some of these regions could potentially be aggregates of PCBM. It would then seem that the inherent self-assembly property of rod-rod block copolymers is detrimental to device performance as is. On the other hand, the gradient copolymer device forms an interconnected structure between the polymer and fullerene leading to higher initial carrier density and improved performance over the block copolymer. Furthermore, our pcAFM study showed that not surprisingly, the P3HT:PCBM sample produced the highest photocurrent, see Fig. S8. A qualitative examination of the 1:1 blend pcAFM image reveals large regions of relatively high photoconductivity similar to P3HT:PCBM, and regions of lower photoconductivity similar to P3HS:PCBM supporting our conclusion of their phase-separated domains.

3. Relevance of Morphology to Device Performance

It is well established that phase separation in polymer:fullerene systems is driven by the crystallization behavior of the polymer.[40, 50] In earlier work we showed that the morphologies and extent of phase separation of thin films of neat P(3HS-*b*-3HT) and P(3HS-*g*-3HT) vary significantly after isothermal recrystallization.[21] As discussed previously in sections 2.3 and 2.4, we attribute the morphological differences observed, to the crystallization behavior of the copolymers, which is driven by the spatial arrangements of the 3HS block/segment along the copolymer chain. Therefore, the BHJ morphology, which influences device performance exhibited in the performance indicators, such as J_{SC}, V_{OC}, *FF* and *PCE*, is guided by the three-dimensional organization of the semicrystalline polymer during the active layer formation and/or subsequent processing procedure. Similarly, for the copolymer devices studied herein, the difference in comonomer sequence distribution along the backbone influences the variation in copolymer crystallization resulting in varying degrees of structural order as shown in our EFTEM and GIXD studies which manifest as differences in device performance. Our results indicate that phase separation in the block copolymer device, driven by the crystallization of the block copolymer, has an adverse effect on device performance, which could be caused by the dense clusters of pure-copolymer domains and an unfavorable morphology. On the other hand, the crystallization behavior of gradient copolymer provides a better nanoscale morphological structure that favors exciton dissociation in the gradient copolymer device.

4. Conclusion

We synthesized an all-conjugated copolymer of 3-hexylselenophene (3HS) and 3-hexylthiophene (3HT) in block and gradient sequence architectures and investigated their structure-performance relationships

as donor materials in organic photovoltaic devices. We found that the comonomer ordering along the copolymer chain influences the optoelectronic properties, nanoscale morphology and device performance in the copolymer:fullerene system. Our EFTEM results show that the block copolymer had a tendency to strongly self-assemble into dense clusters of pure-copolymer rich regions reducing its interfacial area with PCBM. Conversely, the gradient sequence shows an improved control of this innate self-assembly characteristic of copolymers while promoting interfacial activity between the copolymer and fullerene leading to a more continuous and interconnected fibril network with PCBM relative to the block copolymer and as a result generated the highest initial carrier density. All P3HS-containing devices where thermally stable relative to the P3HT-only device and this result was attributed to the higher degree of mixing of PCBM in the P3HS disordered polymer regions thereby suppressing PCBM aggregate growth with annealing.

Copolymer syntheses offer an opportunity through covalently linking comonomers in varying sequences, to merge the valuable properties of homopolymers yielding new and innovative materials. The all-conjugated copolymer approach via molecular design of 3HT and 3HS affords the ability to combine and optimize device efficiency (of P3HT) together with thermal stability (of P3HS) while tailoring BHJ nanoscale morphology. Owing to the rigid backbone and strong rod-rod interactions, fully π-conjugated copolymers behave distinctly different from other classes of copolymers, e.g., rod-coil copolymers. Block copolymers have long served as the material of choice to control nanoscale domain sizes and morphology for organic electronics applications,[51] however, our findings suggest that gradient copolymers could present new opportunities for tailoring the morphology and properties of an all-conjugated copolymer system.

In our study, we have shown that for π-conjugated copolymers that self-assemble and undergo intrinsic phase separation, a gradient sequence along the copolymer backbone could be a potential approach to control and obtain a favorable nanoscale morphology required for optimum performance in photovoltaic systems and possibly other applications, and furthermore combine optoelectronic, physicochemical and thermal properties into one material.

5. Experimental Section

***Polymer Synthesis**:* The copolymers were synthesized and characterized, as recently reported[21] (see Scheme 1). P3HS and P3HT were synthesized following reported procedures.[33, 52] Polymer molecular weights were determined using gel-permeation chromatography (GPC) by comparison with polystyrene standards on a Waters 1515 HPLC instrument equipped with Waters Styragel® (7.8 x 300 mm) THF HR 0.5, THF HR 1, and THF HR 4 type columns in sequence and analyzed with Waters 2487 dual absorbance detector (254 nm). For P3HT, it was found that M_n = 31.2 kDa, $Đ$ = 1.18, regioregularity = 97%; for P3HS, M_n = 23.4 kDa, $Đ$ = 1.21, regioregularity = 98%; for P(3HS-b-3HT) M_n = 26.2 kDa, $Đ$ = 1.14, regioregularity = 97% and for P(3HS-g-3HT) M_n = 32.6 kDa, $Đ$ = 1.18 and regioregularity = 97%. ^{1}H NMR and GPC spectra can be found in the Supporting Information.

Device Fabrication: Indium tin oxide (ITO)-coated aluminosilicate glass slides (Delta Technologies, Ltd.) were cleaned by ultrasonication sequentially in acetone and isopropanol for 20 min. A 4wt% Polyethylenimine, 80% ethoxylated (PEIE) and 2-methoxyethanol (Sigma Aldrich) solution was spin-coated in ambient atmosphere onto the ITO surface at 5000 rpm for 60s, then baked for 10 minutes at 100˚C to form an approximately 10 nm PEIE film. The ITO/PEIE substrates were then transferred into an N2-filled glovebox for device fabrication.

Devices were fabricated in an inverted architecture with the ITO/PEIE as the cathode. P3HT:PCBM (60:40), P3HS:PCBM (50:50), P(3HS-b-3HT):PCBM (55:45), P(3HS-g-3HT):PCBM (55:45) were dissolved in 1,2-dichlorobenzene (*o*-DCB) and stirred in the glovebox

overnight at 80˚C. The solution was then filtered and the active layer spin-coated at 700 rpm for 30 s and thermally annealed at 150˚C for varying times in the glovebox. All P3HS-based samples when spin-coated on preheated substrates at 80˚C. Active layer thicknesses for all samples were in the range of 120 - 140 nm as measured by spectroscopic ellipsometry (M 2000, J.A. Woollam Co.). To complete the device, the anode consisted of 15 nm MoO_3 and 100 nm Ag deposited through a 1 mm diameter shadow mask by vacuum thermal evaporation (Angstrom Engineering PVD system). Devices were then tested in ambient under 1-sun illumination (100 mW cm^{-2}, AM 1.5) using an Oriel solar simulator, and the J-V characteristics were acquired using an Agilent 4156C Semiconductor Parameter Analyzer.

UV-Visible Spectroscopy: UV-vis absorption was measured using a PerkinElmer Lambda 750 Spectrophotometer.

EQE: EQE measurements were performed on devices fabricated in the same manner as described above using collimated light from a halogen lamp coupled to a Newport 1/8m monochromator with a 5 nm FWHM output. The beam was optically chopped at 185 Hz and the photocurrent signal was detected using a Stanford Research Systems SR530 lock-in amplifier and compared to the output from a calibrated Si reference cell.

photo-CELIV: Devices were loaded in a cryostat (Janis VPF-100, vacuum pressure 1 mTorr) and exposed to laser pulses (Quantel BrilliantEazy, λ = 532 nm, pulse intensity ca. 20 μJ cm^{-2}). A function generator (BK Precision 4075) applied a linearly increasing voltage to extract the photo-generated current transient, which was passed through a preamplifier (FEMTO DLPCA-200) and recorded by a digital oscilloscope (Tektronix TDS3052C).

EFTEM: Measurements was performed on a JEOL 2100F TEM, using a slit width of 8 eV and an accelerating voltage of 200 kV. The active layer was spin-coated on a layer of PEDOT:PSS with the same casting and annealing procedures as described in the device fabrication procedure. The films were then sectioned using a razor blade and floated by immersion in deionized water onto copper grids with a supporting mesh (Ted Pella, Inc.).

GIXD: Grazing-incidence X-ray diffraction (GIXD) experiments were run on the G1 line (10.5 +/- 0.1 keV) at the Cornell High Energy Synchrotron Source. The beam was 0.05 mm tall and 1 mm wide. The x-ray beam was aligned such that it is above the critical angle of the polymer:fullerene film but below the critical angle of the substrate. Scattered intensity was collected with a two-dimensional Dectris® Pilatus detector, positioned 86.3 mm from the center of the sample. All images have been background subtracted.

pcAFM: All photoconductive atomic force microscopy (pcAFM) measurements were performed using an Asylum Research MFP-3D stand-alone AFM under ultrapure Ar purge (Cryogenic gases) in a closed fluid cell. A Pt/Ir_5-coated contact-mode AFM probe (Nanosensors, ATEC-CONTPt, spring constant 0.2 N/m) was used as the top contact allowing simultaneous determination of both topography and photocurrent recorded using the AFM's transimpedance amplifier. The source of illumination was a 532 nm diffraction limited laser focused and aligned to the probe, using a bottom-mounted objective. The illumination intensity was on the order of 10^4 W/m^2 for all devices.

Conflicts of interest

The authors declare no competing financial interest.

Acknowledgements

This work was partially supported by the Center for Solar and Thermal Energy Conversion at the University of Michigan (Department of Energy, Energy Frontier Research Center, Award No. DE-SC0000957, (JAA, AL, MES, BH, EFP, AJM, MS, PFG), and the National Defense Science and Engineering Graduate Fellowship, Office of Naval Research (GP). This work is based upon research conducted at the Cornell High Energy Synchrotron Source (CHESS), which is supported, by the National Science Foundation and the National Institutes of Health/National Institute of General Medical Sciences under NSF awards DMR-0936384 and DMR-1332208.

References

1. J. Peet, J. Y. Kim, N. E. Coates, W. L. Ma, D. Moses, A. J. Heeger and G. C. Bazan, *Nat Mater*, 2007, **6**, 497.
2. X. N. Yang, J. Loos, S. C. Veenstra, W. J. H. Verhees, M. M. Wienk, J. M. Kroon, M. A. J. Michels and R. A. J. Janssen, *Nano Lett*, 2005, **5**, 579.
3. B. C. Thompson and J. M. J. Frechet, *Angew Chem Int Edit*, 2008, **47**, 58.
4. J. B. Kim, K. Allen, S. J. Oh, S. Lee, M. F. Toney, Y. S. Kim, C. R. Kagan, C. Nuckolls and Y. L. Loo, *Chem Mater*, 2010, **22**, 5762.
5. E. F. Palermo, S. B. Darling and A. J. McNeil, *J Mater Chem C*, 2014, **2**, 3401.
6. S. Bertho, G. Janssen, T. J. Cleij, B. Conings, W. Moons, A. Gadisa, J. D'Haen, E. Goovaerts, L. Lutsen, J. Manca and D. Vanderzande, *Sol Energ Mat Sol C*, 2008, **92**, 753.
7. N. D. Treat, M. A. Brady, G. Smith, M. F. Toney, E. J. Kramer, C. J. Hawker and M. L. Chabinyc, *Adv Energy Mater*, 2011, **1**, 145.
8. G. Griffini, J. D. Douglas, C. Piliego, T. W. Holcombe, S. Turri, J. M. J. Frechet and J. L. Mynar, *Adv Mater*, 2011, **23**, 1660.
9. Y. Lin, J. A. Lim, Q. S. Wei, S. C. B. Mannsfeld, A. L. Briseno and J. J. Watkins, *Chem Mater*, 2012, **24**, 622.
10. Y. J. Cheng, C. H. Hsieh, P. J. Li and C. S. Hsu, *Adv Funct Mater*, 2011, **21**, 1723.
11. D. Gao, J. Hollinger and D. S. Seferos, *Acs Nano*, 2012, **6**, 7114.
12. J. U. Lee, J. W. Jung, T. Emrick, T. P. Russell and W. H. Jo, *J Mater Chem*, 2010, **20**, 3287.
13. K. Sivula, C. K. Luscombe, B. C. Thompson and J. M. J. Frechet, *J Am Chem Soc*, 2006, **128**, 13988.
14. A. Li, J. Amonoo, B. Y. Huang, P. K. Goldberg, A. J. McNeil and P. F. Green, *Adv Funct Mater*, 2014, **24**, 5594.
15. M. He, W. Han, J. Ge, Y. L. Yang, F. Qiu and Z. Q. Lin, *Energ Environ Sci*, 2011, **4**, 2894.
16. K. C. Gallow, Y. K. Jhon, J. Genzer and Y. L. Loo, *Polymer*, 2012, **53**, 1131.
17. K. C. Gallow, Y. K. Jhon, W. Tang, J. Genzer and Y. L. Loo, *J Polym Sci Pol Phys*, 2011, **49**, 629.
18. L. S. Li, J. Hollinger, N. Coombs, S. Petrov and D. S. Seferos, *Angew Chem Int Edit*, 2011, **50**, 8148.
19. J. Hollinger, A. A. Jahnke, N. Coombs and D. S. Seferos, *J Am Chem Soc*, 2010, **132**, 8546.
20. Z. J. Bryan and A. J. McNeil, *Macromolecules*, 2013, **46**, 8395.
21. E. F. Palermo and A. J. McNeil, *Macromolecules*, 2012, **45**, 5948.
22. J. R. Locke and A. J. McNeil, *Macromolecules*, 2010, **43**, 8709.
23. E. F. Palermo, H. L. van der Laan and A. J. McNeil, *Polym Chem-Uk*, 2013, **4**, 4606.
24. S. Okabe, K. Seno, S. Kanaoka, S. Aoshima and M. Shibayama, *Macromolecules*, 2006, **39**, 1592.
25. S. Okabe, K. Seno, S. Kanaoka, S. Aoshima and M. Shibayama, *Polymer*, 2006, **47**, 7572.
26. N. Merlet-Lacroix, E. Di Cola and M. Cloitre, *Soft Matter*, 2010, **6**, 984.
27. J. Kim, R. W. Sandoval, C. M. Dettmer, S. T. Nguyen and J. M. Torkelson, *Polymer*, 2008, **49**, 2686.
28. J. Kim, H. Y. Zhou, S. T. Nguyen and J. M. Torkelson, *Polymer*, 2006, **47**, 5799.
29. J. Kim, M. M. Mok, R. W. Sandoval, D. J. Woo and J. M. Torkelson, *Macromolecules*, 2006, **39**, 6152.
30. P. Hodrokoukes, G. Floudas, S. Pispas and N. Hadjichristidis, *Macromolecules*, 2001, **34**, 650.
31. Z. Xu, L. M. Chen, G. W. Yang, C. H. Huang, J. H. Hou, Y. Wu, G. Li, C. S. Hsu and Y. Yang, *Adv Funct Mater*, 2009, **19**, 1227.
32. A. M. Ballantyne, L. C. Chen, J. Nelson, D. D. C. Bradley, Y. Astuti, A. Maurano, C. G. Shuttle, J. R. Durrant, M. Heeney, W. Duffy and I. McCulloch, *Adv Mater*, 2007, **19**, 4544.
33. M. Heeney, W. Zhang, D. J. Crouch, M. L. Chabinyc, S. Gordeyev, R. Hamilton, S. J. Higgins, I. McCulloch, P. J. Skabara, D. Sparrowe and S. Tierney, *Chem Commun*, 2007, DOI: Doi 10.1039/B712398a, 5061.
34. G. Li, V. Shrotriya, J. S. Huang, Y. Yao, T. Moriarty, K. Emery and Y. Yang, *Nat Mater*, 2005, **4**, 864.
35. J. Hollinger, P. M. DiCarmine, D. Karl and D. S. Seferos, *Macromolecules*, 2012, **45**, 3772.
36. W. C. Tsoi, D. T. James, E. B. Domingo, J. S. Kim, M. Al-Hashimi, C. E. Murphy, N. Stingelin, M. Heeney and J. S. Kim, *Acs Nano*, 2012, **6**, 9646.
37. S. Lilliu, T. Agostinelli, E. Verploegen, E. Pires, M. Hampton, M. Al-Hashimi, M. J. Heeney, M. F. Toney, J. Nelson and J. E. Macdonald, *Macromol Rapid Comm*, 2011, **32**, 1454.
38. J. Hollinger and D. S. Seferos, *Macromolecules*, 2014, **47**, 5002.
39. J. Ge, M. He, N. Xie, X. B. Yang, Z. Ye and F. Qiu, *Macromolecules*, 2015, **48**, 279.
40. D. R. Kozub, K. Vakhshouri, L. M. Orme, C. Wang, A. Hexemer and E. D. Gomez, *Macromolecules*, 2011, **44**, 5722.
41. D. Gao, J. Hollinger, A. A. Jahnke and D. S. Seferos, *J Mater Chem A*, 2014, **2**, 6058.
42. N. B. Tito, S. T. Milner and J. E. G. Lipson, *Macromolecules*, 2010, **43**, 10612.
43. M. D. Lefebvre, M. O. de la Cruz and K. R. Shull, *Macromolecules*, 2004, **37**, 1118.
44. S. R. Cowan, A. Roy and A. J. Heeger, *Phys Rev B*, 2010, **82**.
45. A. Maurano, R. Hamilton, C. G. Shuttle, A. M. Ballantyne, J. Nelson, B. O'Regan, W. M. Zhang, I. McCulloch, H. Azimi, M. Morana, C. J. Brabec and J. R. Durrant, *Adv Mater*, 2010, **22**, 4987.
46. A. Maurano, C. C. Shuttle, R. Hamilton, A. M. Ballantyne, J. Nelson, W. M. Zhang, M. Heeney and J. R. Durrant, *J Phys Chem C*, 2011, **115**, 5947.

47. C. G. Shuttle, B. O'Regan, A. M. Ballantyne, J. Nelson, D. D. C. Bradley and J. R. Durrant, *Phys Rev B*, 2008, **78**.
48. S. Sweetnam, K. R. Graham, G. O. N. Ndjawa, T. Heumuller, J. A. Bartelt, T. M. Burke, W. T. Li, W. You, A. Amassian and M. D. McGehee, *J Am Chem Soc*, 2014, **136**, 14078.
49. I. Lange, J. Kniepert, P. Pingel, I. Dumsch, S. Allard, S. Janietz, U. Scherf and D. Neher, *J Phys Chem Lett*, 2013, **4**, 3865.
50. S. Lilliu, T. Agostinelli, E. Pires, M. Hampton, J. Nelson and J. E. Macdonald, *Macromolecules*, 2011, **44**, 2725.
51. R. A. Segalman, B. McCulloch, S. Kirmayer and J. J. Urban, *Macromolecules*, 2009, **42**, 9205.
52. R. D. McCullough, *Adv Mater*, 1998, **10**, 93.

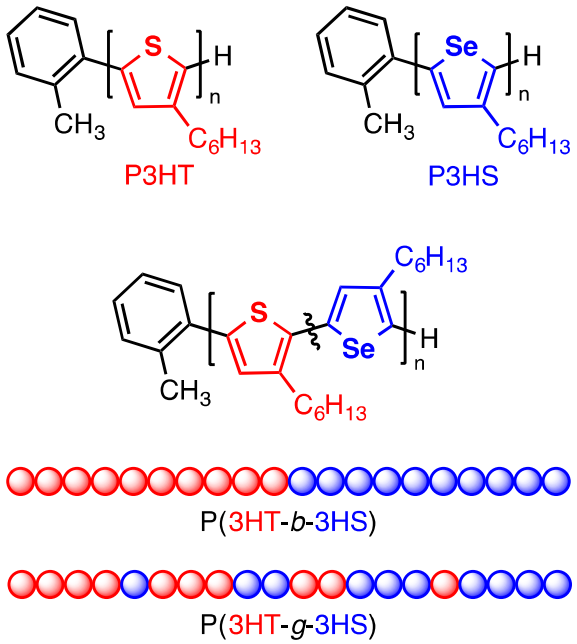

Fig. 1 Chemical structure of the polymers and copolymers used in this work

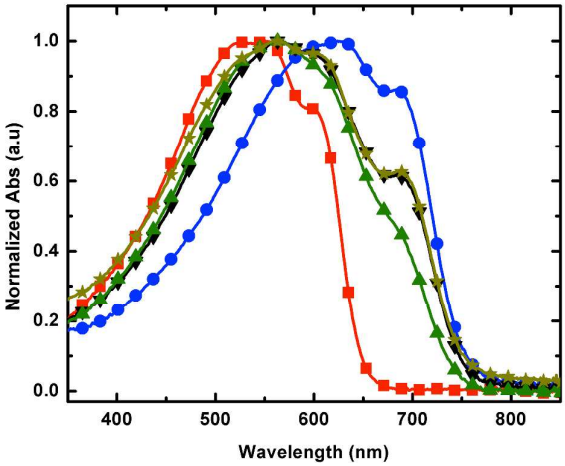

Fig. 2 UV-vis absorption spectra of optimized samples of P3HT:PCBM (red, square), P3HS:PCBM (blue circle), P3HS:P3HT:(1:1)PCBM (dark yellow star), P(3HS-*b*-3HT):PCBM (black inverted triangle) and P(3HS-*g*-3HT):PCBM (green triangle).

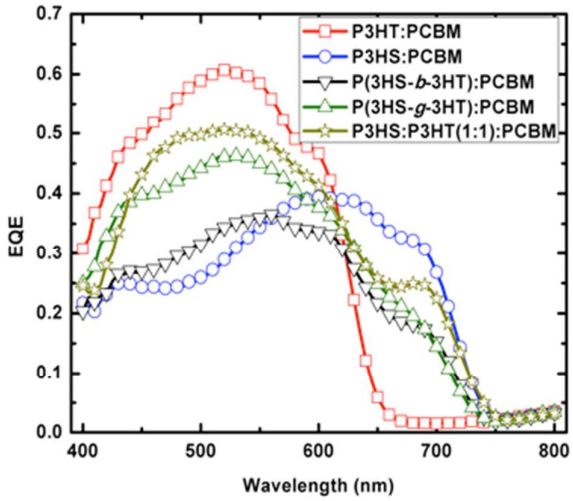

Fig. 3 External quantum efficiency spectra of optimized devices of P3HT:PCBM (red square), P3HS:PCBM (blue circle), P3HS:P3HT:(1:1)PCBM (dark yellow star), P(3HS-*b*-3HT):PCBM (black inverted triangle) and P(3HS-*g*-3HT):PCBM (green triangle).

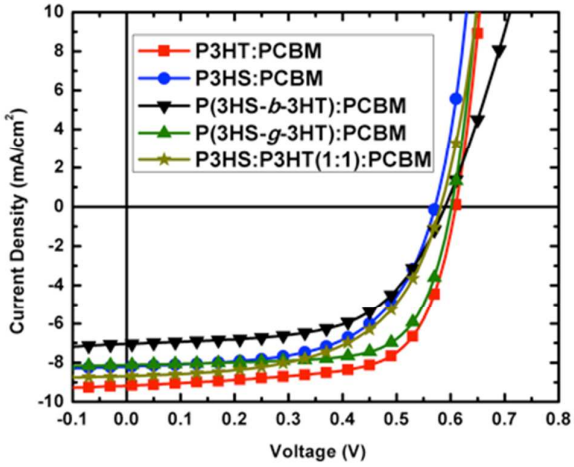

Fig. 4 Current density-Voltage (J-V) curves of optimized devices of P3HT:PCBM (red square), P3HS:PCBM (blue circle), P3HS:P3HT:(1:1)PCBM (dark yellow star), P(3HS-*b*-3HT):PCBM (black inverted triangle) and P(3HS-*g*-3HT):PCBM (green triangle).

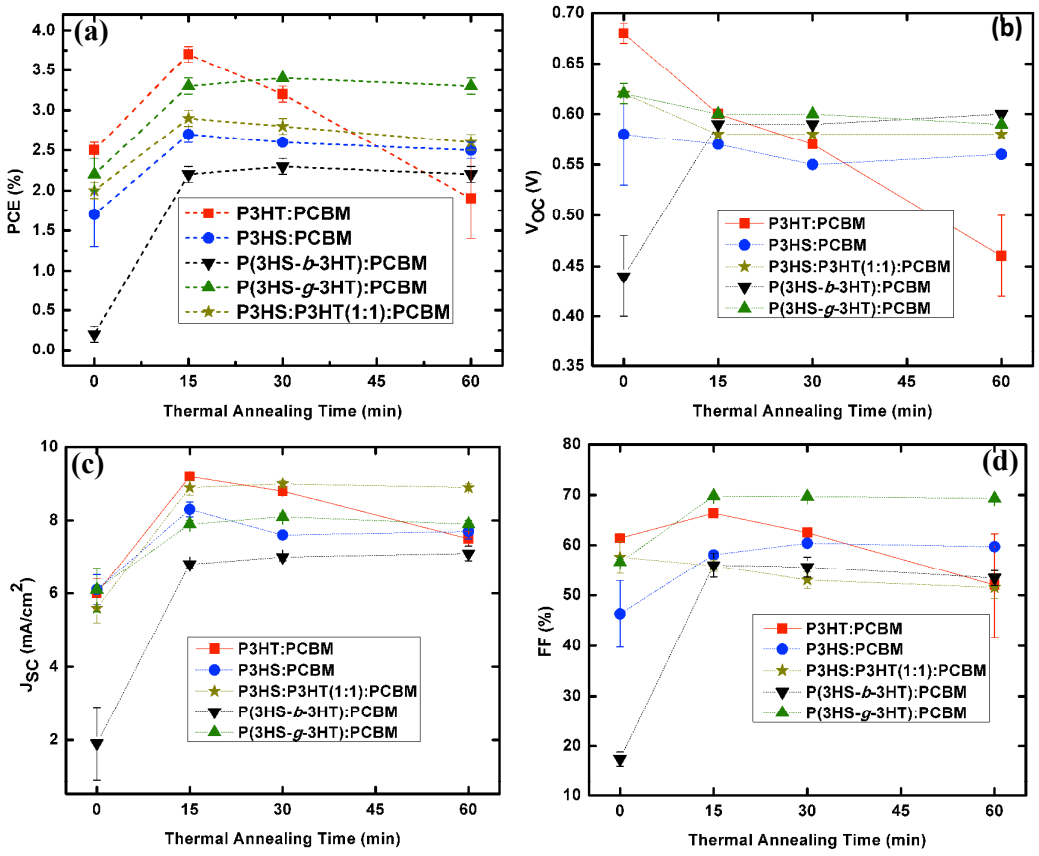

Fig. 5 Plots of (a) Power conversion efficiency (PCE) (b) Open circuit voltage (V_{OC}) (c) Short circuit current (J_{SC}) and (d) Fill factor (*FF*) as a function of annealing time at 150°C for P3HT:PCBM (red square), P3HS:PCBM (blue circle), P3HS:P3HT:(1:1)PCBM (dark yellow star), P(3HS-*b*-3HT):PCBM (black inverted triangle) and P(3HS-*g*-3HT):PCBM (green triangle).

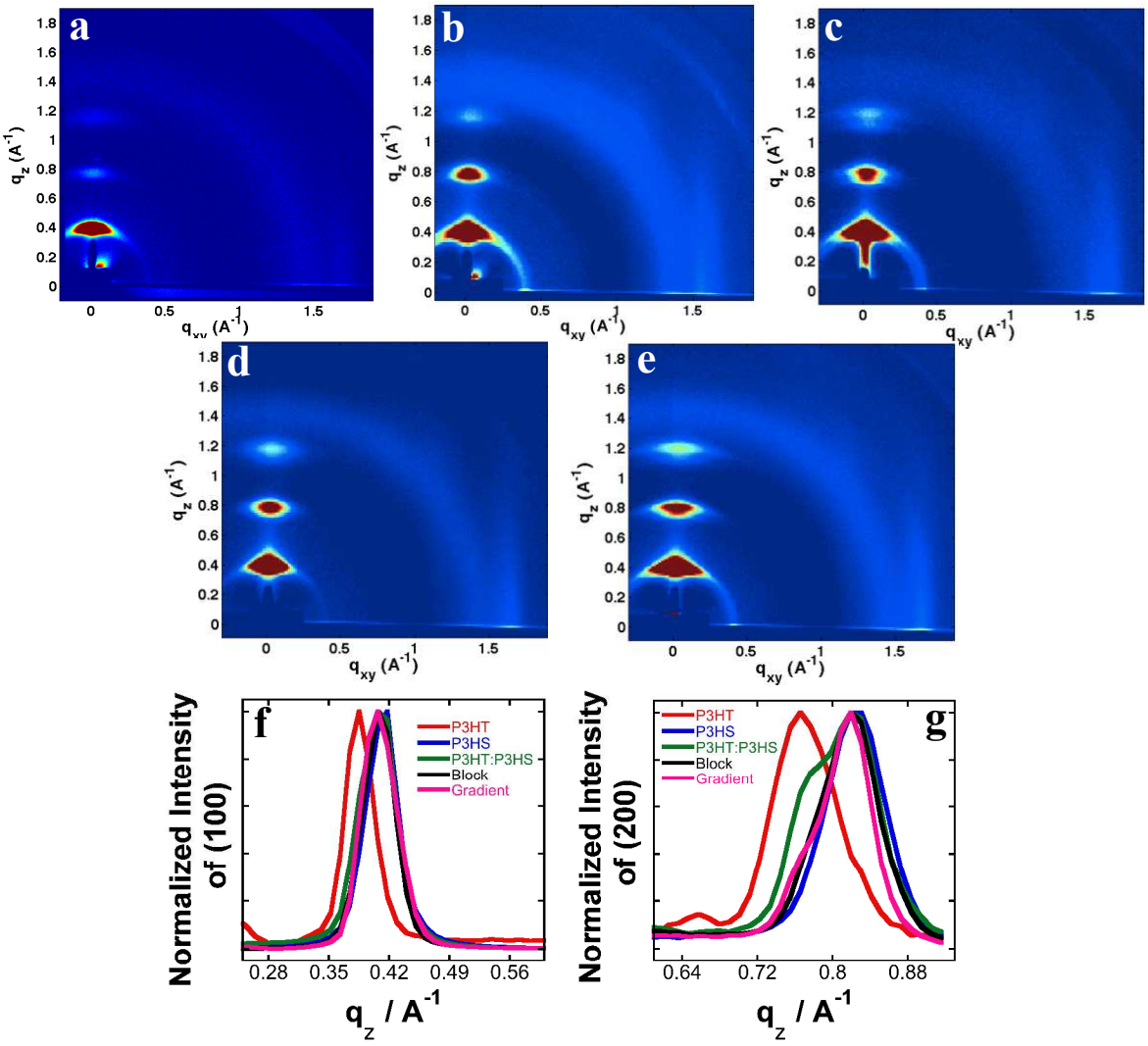

Fig. 6 Grazing Incidence X-ray Diffraction (GIXRD) patterns of optimum samples of (a) P3HT:PCBM (b) P3HS:PCBM (c) P3HS:P3HT:(1:1)PCBM), and (d) P(3HS-*b*-3HT):PCBM, (e) P(3HS-*g*-3HT):PCBM. Normalized intensity traces taken at q_{xy} = 0, indicative of the (100) and (200) reflections (f and g, respectively).

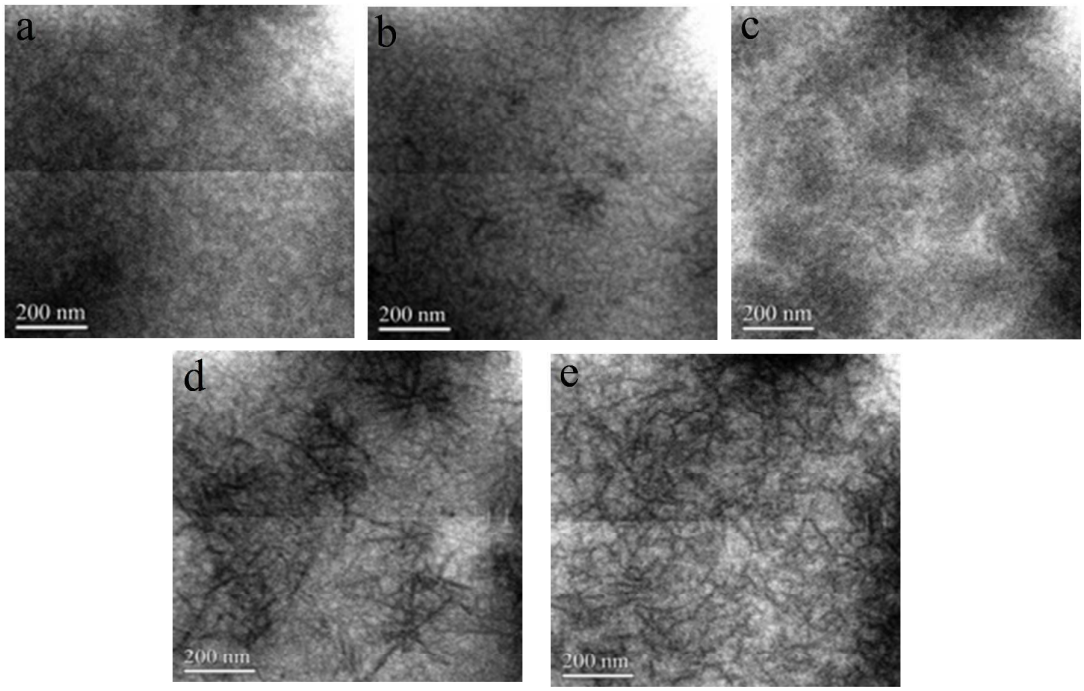

Fig. 7 Energy-filtered transmission electron microscopy (EFTEM) images of (a) P3HT:PCBM (b) P3HS:PCBM (c) P3HS:P3HT:(1:1)PCBM), and (d) P(3HS-*b*-3HT):PCBM and (e) P(3HS-*g*-3HT):PCBM. The energy window is selected such that the polymer-rich phase is dark.

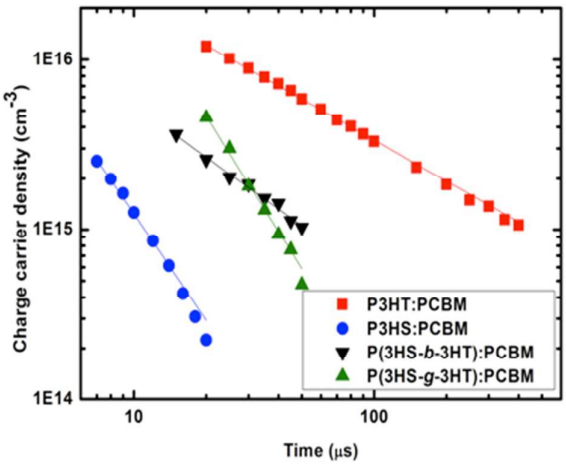

Fig. 8 Concentration of extracted photogenerated charge carriers as a function of delay time measured by photo-CELIV for optimized devices of P3HT:PCBM (red square), P3HS:PCBM (blue circle), P(3HS-*b*-3HT):PCBM (black inverted triangle) and P(3HS-*g*-3HT):PCBM (green triangle).

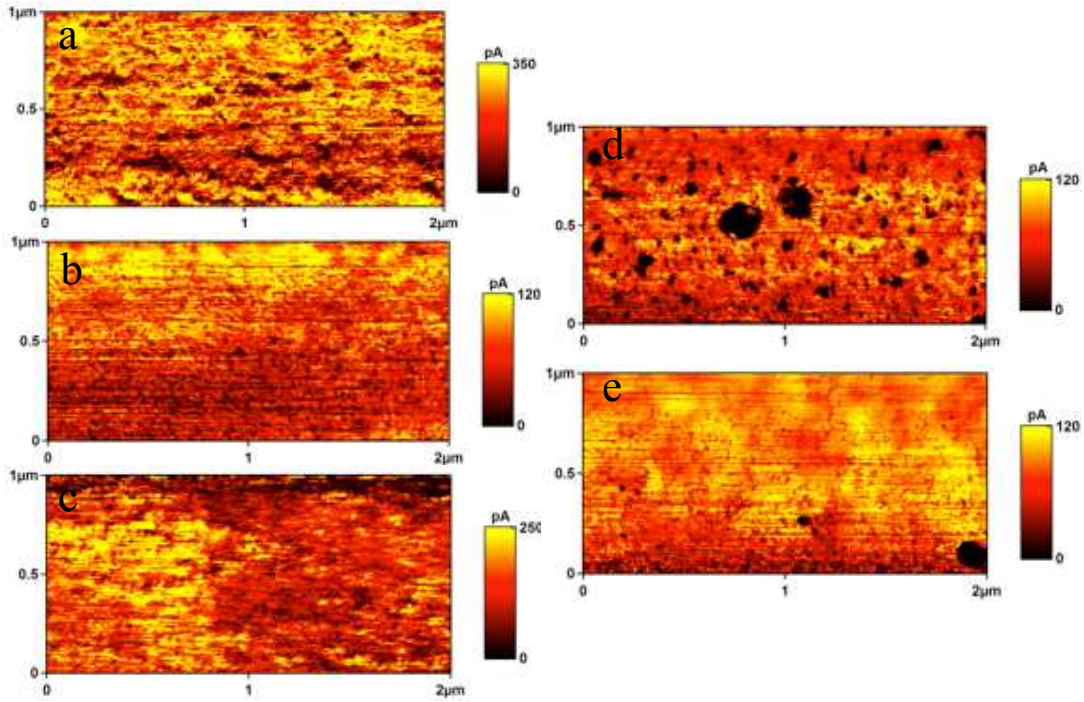

Fig. 9 Photocurrent images from photoconductive AFM of (a) P3HT:PCBM (b) P3HS:PCBM (c) P3HS:P3HT:(1:1)PCBM), and (d) P(3HS-*b*-3HT):PCBM and (e) P(3HS-*g*-3HT):PCBM.

Table of contents entry:

A larger interfacial area between the copolymer and fullerene is obtained with the gradient copolymer relative to the block architecture. This is correlated with two orders of magnitude higher initial carrier density.

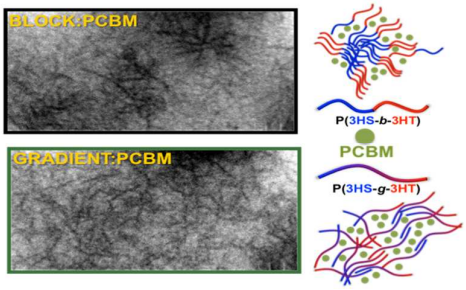

Table of contents graphic